Energy signature of ton TNT-class impacts: analysis of the 22 December 2018 fireball over Western Pyrenees

S Anghel, E Drolshagen, T Ott, M Birlan, F Colas, D Nedelcu, D Koschny, B Zanda, S Bouley, S Jeanne, et al.

Monthly Notices of the ROYAL ASTRONOMICAL SOCIETY

MNRAS **508,** 5716–5733 (2021) https://doi.org/10.1093/mnras/stab2968
Advance Access publication 2021 October 18

Energy signature of ton TNT-class impacts: analysis of the 2018 December 22 fireball over Western Pyrenees

S. Anghel [1,2,3★] E. Drolshagen,[4] T. Ott,[4] M. Birlan,[1,2★] F. Colas,[2] D. A. Nedelcu,[1,2] D. Koschny,[5] B. Zanda,[2,6] S. Bouley,[2,7] S. Jeanne,[2] A. Malgoyre,[8] C. Blanpain,[8] J. Gattacceca,[9] L. Jorda,[10] J. Lecubin,[8] J. L. Rault,[2] J. Vaubaillon [2] P. Vernazza,[10] R. Hueso,[11,12] E. Peña-Asensio,[13,14,15] S. J. Ribas,[16,17] A. Rimola [13] A. Sánchez-Lavega,[11,12] M. Tapia,[18] J. M. Trigo-Rodriguez [14,15] P. Cauhape,[19] C. Davadan,[20] P. Dupouy,[21] M. Herpin,[19] D. Rousseu[19] and B. Tregon[22]

Affiliations are listed at the end of the paper

Accepted 2021 October 10. Received 2021 September 9; in original form 2021 June 25

ABSTRACT

The increase in detector sensitivity and availability in the past three decades has allowed us to derive knowledge of the meteoroid flux and impact energy into the Earth's atmosphere. We present the multi-instrument detected 2018 December 22 fireball over Western Pyrenees, and compare several techniques aiming to obtain a reliable method to be used when measuring impacts of similar scale. From trajectory data alone, we found a bulk density of 3.5 g cm^{-3} to be the most likely value for the Pyrenean meteoroid. This allowed to further constrain the dynamic mass, which translated into a kinetic energy of 1 ton TNT (4.184×10^9 J). For the second energy derivation, via the fireball's corrected optical radiation, we obtained a more accurate empirical relation measuring well-studied bolides. The result approximates to 1.1 ton TNT, which is notably close to the nominal dynamic result, and agrees with the lower margin of the seismic-based energy estimation, yet way lower than the infrasound estimate. Based on the relation derived in this study, we consider the nominal estimate from both the dynamic and photometric methods to be the most accurate value of deposited energy (1 ton TNT). We show that the combination of these two methods can be used to infer the meteoroid density. Among the methods presented in this paper, we found that the optical energy is the most reliable predictor of impact energy near the ton TNT-scale.

Key words: techniques: photometric – meteorites, meteors, meteoroids – minor planets, asteroids: general.

1 INTRODUCTION

Fireball records are becoming a routine scientific program. All-sky and wide-field networks (e.g. Trigo-Rodriguez et al. 2008; Jenniskens et al. 2011; Cooke & Moser 2012; Gritsevich et al. 2014; Toth et al. 2018; Koseki 2019; Colas et al. 2020; Devillepoix et al. 2020; Vida et al. 2021) are now detecting meteors daily around the World. From the most energetic events recorded (i.e. bolides), few meteoroids survive the harsh atmospheric entry and reach the ground, and of those, only a small fraction are found as meteorites. Until now, there are roughly 1200 meteorite falls[1] that have been officially documented and classified according to their type. Among those, there are only 40 with available instrumentally derived trajectory and orbital data (table 1 of Colas et al. 2020), thus making them a treasure of information, which provides answers concerning the history and evolution of the Solar system.

When an object collides with the Earth's atmosphere, it produces a wide range of phenomena such as heat, light, ionization, atmospheric shocks (Silber & Brown 2014). These phenomena could be detected by observation networks via several instruments (optical, radar, infrasound). However, due to a broad variation in meteoroid size, internal structure, and entry geometry, there are few recorded events that agree well on impact energy estimations. Still, a combination of accurate multi-instrumental data, with a focus on trajectory, will introduce constraints on the physical properties of the corresponding meteoroid. Peaks on the light curve indicate fragmentation events that reveal aspects like meteoroid structure and bulk strength (Borovička, Spurný & Shrbený 2020). Good tracking along the trajectory for each fragment is important when analysing the radiated energy (Spurný, Borovička & Shrbený 2020). Careful tracking is essential also to constrain the strewn field (Moilanen, Gritsevich & Lyytinen 2021), thus decreasing the meteorite search time. Supplementary radar recordings contribute to a better velocity approximation (table 4 of Colas et al. 2020), which translates into a constraint for the semimajor axis, which in turn is important when analysing source regions in the main belt.

Upon atmospheric impact, a pressure change will be generated. This signal propagates in the atmosphere and can be detected in the infrasound range even after large distances, before dissipation. This has been shown in several publications, see e.g. Ens et al. (2012), Hedlin et al. (2012), Silber, Le Pichon & Brown (2011), Caudron et al. (2016), Ott et al. (2019), or Pilger et al. (2020). The largest and probably best-known example is the Chelyabinsk superbolide in 2013. This fireball was detected by infrasound stations worldwide, of

★ E-mail: simon.anghel@astro.ro (SA); Mirel.Birlan@obspm.fr (MB)
[1] https://www.lpi.usra.edu/meteor/metbull.php

Table 1. The coordinates of the stations that were used in this analysis.

Location	Code	Lat (°)	Lon (°)	Alt (m)
Dax, FR	FRAQ04	43.693	−1.030	36
Hendaye, FR	FRAQ03	43.377	−1.749	87
Montsec, ES	ESCA01	42.024	0.737	820
Alkurruntz, ES	EALK	43.220	−1.507	965
Aranguren, ES	EARA	42.773	−1.579	476
Chisagües, ES	ECHI	42.665	0.195	1450
San Caprasio, ES	ESAC	41.722	−0.469	815
Kesra, TN	I48TN	35.81*	9.32*	852*

*The value is the average coordinate of the detectors which make up the infrasound station's array.

which 20 International Monitoring System (IMS) facilities showed a clearly recorded signal (Brown et al. 2013; Le Pichon et al. 2013; Pilger et al. 2015). The work by Gi & Brown (2017) includes more than 70 Near-Earth Objects (NEOs) impacts that were recorded with infrasound stations. Today, meteor generated infrasound is a topic of current research. For more information about the background and method, the reader is referred to e.g. Silber et al. (2018) or Ott et al. (2019).

From the infrasound data it is possible to compute the impact location, energy, and approximate entry mass of the meteoroid or asteroid. For some fireball events, information is available in different kinds of data sources. These sources can range from witness reports, like the AMS/IMO (American Meteor Society/International Meteor Organization) service (Hankey & Perlerin 2015 and AMS/IMO, 2020), to fireball networks like FRIPON, up to lightning detectors in space (Jenniskens et al. 2018). Combining e.g. the meteor velocity computed by a fireball network, with the energy derived from the infrasound data can yield a more precise mass and size estimation for the entering object. Furthermore, with a combination of data sources, it is possible to investigate the different detection methods themselves. For details and examples, the reader is referred to e.g. Ott et al. (2019, 2020).

Recently, a global near real-time fireball monitoring system was developed among others for this purpose, and is in operation at ESA (European Space Agency) as part of its Space Safety Programme. It is called NEMO (NEar real-time MOnitoring system) and combines data from multiple sources. It consists of an alert procedure based on social media, to produce rapid notifications of fireball events which generate wide public attention (Ott et al. 2020). This is an important step towards big data science, as bringing together multiple reports of the same object can improve our understanding of the phenomenon.

During the next two sections, we present the methods applied when analysing the instrumentally observed Pyrenean fireball and the results obtained. In Section 4, we derive an empirical relation for fireball source energy based on well-studied events, and compare it with other methods of obtaining the impact energy applied to similar scale events. In Section 5, we discuss the importance of complementary data to better understand a phenomenon. In the final section, we present the conclusions of this study and the implications for future work.

2 CONTEXT AND METHODS

At 21:12 UT (22:12 local time) on 2018 December 22, a bright fireball was observed over southern France and Spain (Fig. 1). Multiple casual observers (as far as 600 km from the terminal point) reported

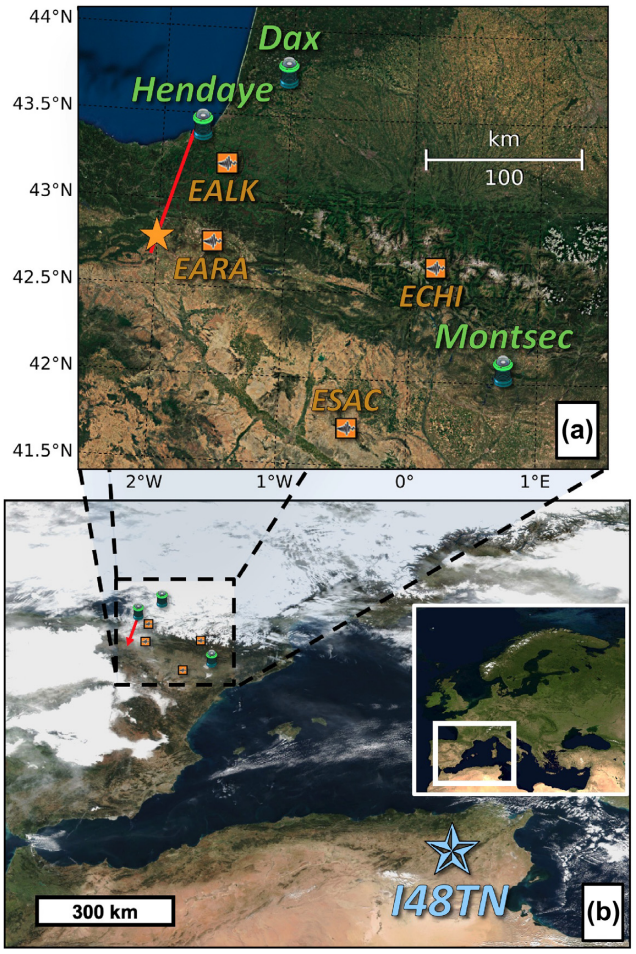

Figure 1. Satellite view of the Western Mediterranean. The ground projection of the fireball is represented by the red line and the main ablation by the orange star (image A). FRIPON stations that captured the event are marked with green. The airwave was detected at four seismic stations of the IGN (orange), and one infrasound station of the IMS (blue). B displays the cloud distribution around the time of the fireball, while A presents a clear sky context, to better convey the location of the stations. The maps were extracted using the Matplotlib Basemap Toolkit and NASA Worldview platform.

the event on IMO website and on social platforms (e.g. https://www.vigie-ciel.org/). A search to recover the meteorite was organized by teams of FRIPON, Institute of Space Sciences (CSIC-IEEC), Planetarium of Pamplona, SPanish Meteor Network (SPMN), and Universidad de Navarra. The search covered a surface of 2 km^2 at 15 km east of Logroño (La Rioja, Spain); no meteorite was found.

A strong thunder-like sound was reported by witnesses some seconds after the event, in the central region of Navarra (Yanguas et al. 2019). The acoustic waves coupled to the Earth's surface, and were detected as seismic signal on four stations of the Spanish seismic network of the Instituto Geográfico Nacional (IGN). Airwave signal was detectable for at least 2000 km from the fireball, as it reached a high signal-to-noise ratio on I48TN IMS infrasound station, located in Kesra, Tunisia (Table 1). The fireball was also detected for 5 s in the silicon pass band (400–1100 nm wavelength) of three FRIPON cameras, through various thicknesses of cloud coverage (Fig. 2).

At the time of the fireball, France was under full cloud coverage (Fig. 1), and the sky was illuminated by a full Moon, impeding other stations to detect the fireball. From Dax, France, the fireball

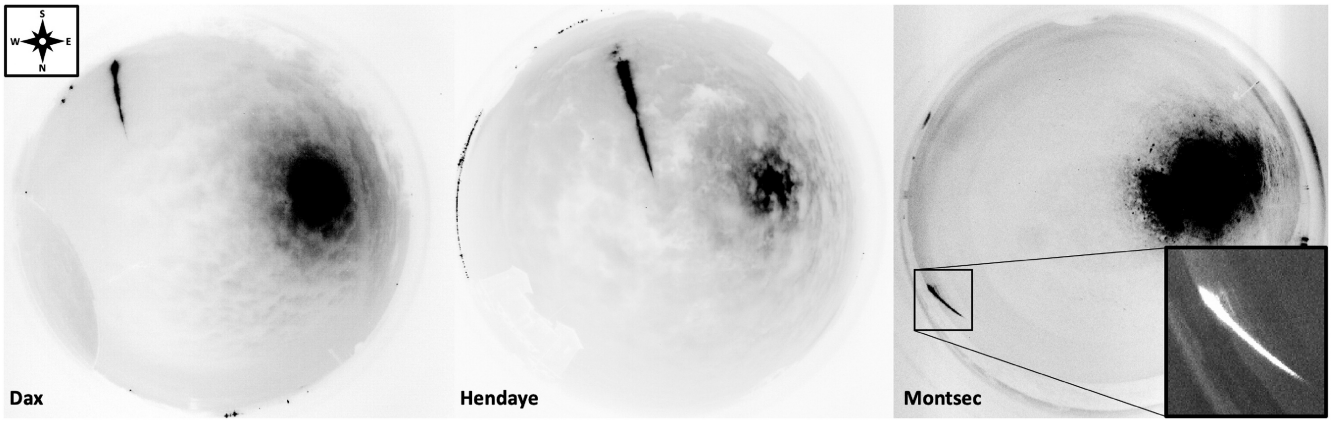

Figure 2. Mosaic of composite frames of the FRIPON all-sky cameras involved in the event analysis. The images were inverted, and a part of the corresponding original is displayed in the zoomed luminous path as seen from the Montsec station. The image orientation is indicated by the compass rose in the upper left. The dark patch in the middle-right part of each image is the full moon (100 per cent illuminated during the event). The variation in moon and fireball luminosity between images is produced by different levels of cloud coverage (i.e. overcast sky of varying thickness for both Dax and Hendaye; clear sky for Montsec). Seen from Montsec, the fireball finished the luminous trajectory just before the line of sight (mountain ridge at horizon), yet well above the cloud layer.

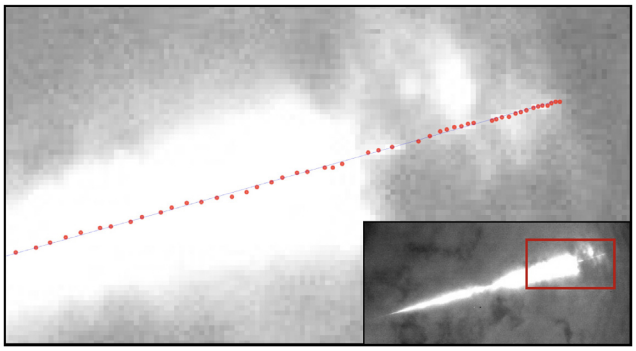

Figure 3. Ending of the fireball as seen by the digital all-sky camera at the Hendaye station. The background picture is a composite of frames involved in the detection. The red dots are centroid measurements on frames (30 fps), while the thin central line is the linear regression of the apparent trajectory. Note the rapid increase in centroid frequency towards the end part, due to deceleration. There are a few frame measurements missing towards the very end, due to heavy extinction induced by clouds.

was observed through a fairly uniform layer of clouds, while on the Montsec station, Spain, the entire luminous trajectory was seen well above the clouds, and ended right before the horizon.

Hendaye, France, hosts the closest FRIPON camera from the atmospheric entry. From this station, the object was seen through an uneven layer of clouds (altocumulus), varying in thickness along the trajectory. On the one hand, a uniform layer of clouds can be beneficial for astrometric measurements of bright events (Fig. 3). On the other hand, as described below, when modelling the meteoroid's energy release, an additional set of calibrations is required. The image data along with camera orientation are displayed in Fig. 2.

2.1 Optical data

For astrometry and photometry, we used the data recorded by three automated digital cameras of FRIPON. The cameras are based on the CCD Sony ICX445 chip (1.2 Mp resolution, 12 bits), operating at 30 frames s^{-1} (Colas et al. 2014). Currently, the FRIPON network and extensions assemble more than 150 stations installed around the world, most of which are located in Western Europe (Gardiol, Cellino & Di Martino 2016; Koschny et al. 2018; Nedelcu et al. 2018; Colas et al. 2020).

FREETURE open source software (Audureau et al. 2014) was implemented across the network for meteor detection and long exposure acquisition (captures). Next, data are reduced by the FRIpon PIPEline (FRIPIPE) automatic routines, to obtain the orbit, trajectory, dark flight, and strewn field (Vaubaillon et al. 2018). Additionally, as described in Sections 2.1.1 and 3.1.1, recent FRIPIPE updates allow a better tracking along the atmosphere, and dynamic mass estimates.

2.1.1 Astrometry

A meteor detection delivers a set of 33 μs frames (30 fps) in FITS format. There are hardly any stars visible on this sequence, thus FREETURE acquires a 5 s exposure *capture* every 10 min. Each *capture* will produce a set of reference stars (hundreds of stars for dark sites), which will serve for astrometric and photometric calibrations.

The astrometric solution is generated for each camera location from a month-long set of *captures*. The goal is to convert CCD Cartesian coordinates (x,y) into horizontal coordinates. This procedure is modelled using 12 parameters that take into account the orientation of the camera, the optical centre position, a radial distortion function, and an empirical factor for asymmetry. The complete model is detailed by Jeanne et al. (2019).

FREETURE's automated procedure delivers a rough estimation of the meteor centroid for a selection of frames. To ensure a proper analysis of the event, all the frames were measured manually. The meteor trajectory is built by separating time and space coordinates, and assuming it to be a straight line, as described by Ceplecha (1987). Next, a modified sum of residuals is applied to the least-squares method (Borovička 1990), which assigns a weight to each camera, depending on the accuracy of the calibration, the number of images, and measurement noise. The full description and application of this model is presented by Jeanne et al. (2019).

2.1.2 Photometry

The flux was obtained by summing the background subtracted pixel values for each frame of the detection. In Fig. 4, we take the flux

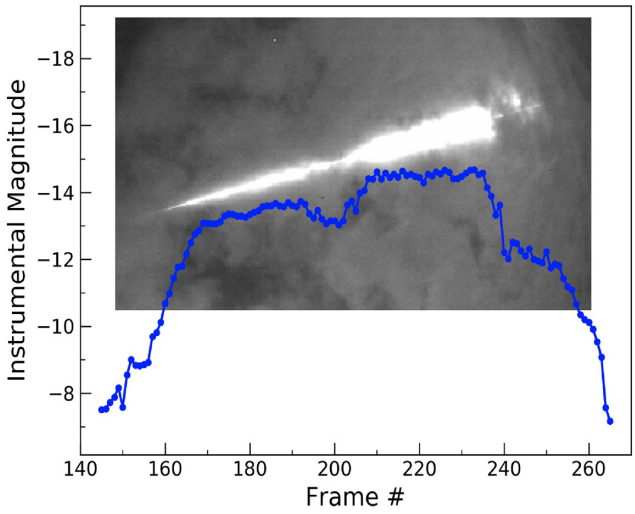

Figure 4. The Western Pyrenees fireball uncalibrated instrumental magnitude seen from the Hendaye station in each frame of the detection. The plot is superimposed on the meteor region of interest, built from stacked frames. Notice the absorption due to the change in cloud thickness along the trajectory.

common logarithm from Hendaye, and multiply by −2.5 to obtain the instrumental magnitude. To convert it into absolute units, we corrected for distance and extinction.

Depending on the station, the extinction coefficient can change also as a function of azimuth (Anghel et al. 2019). None the less, during the week prior to the event, there were no major dichotomies found along the azimuth, so a generic all sky extinction was used.

FRIPIPE computations allow an initial absolute light curve of the fireball (Jeanne et al. 2019; Colas et al. 2020). The limitation of this photometric routine resides in dealing with saturated images. In fact, for this event, most of the recorded frames are saturated. This will affect the measurements of luminosity and will diminish the real photometry of the fireball.

For our current configuration (Colas et al. 2014), a fireball with an absolute magnitude of −8 will start to saturate the cameras at ≈ 80 km distance. To reconstruct the missing light due to saturation, a routine was developed (see logical scheme: Section A) that corrects the flux on all-sky cameras based on the model similar to the one described by Kikwaya et al. (2010). Its operation in an automated network requires a clear sky from at least two stations, yet during the Pyrenean fireball, an unobstructed luminosity measurement was only possible from Montsec. As the automated model had poor applicability in this scenario, we adapted it to a particular case, where clouds act as a natural filter, allowing only a part of fireball radiation to reach the detector.

During uniform clouds, the otherwise clipped bolide highlight (i.e. on clear sky) is replaced by a dimmed point spread function (PSF) with a clear centroid (Fig. 5). This will favour the astrometric and photometric measurements, by better constraining the position of the object and its change in brightness (see Section 3.2).

Here, two trade-offs are introduced; small detaching fragments will not be visible through clouds, and variable cloud thickness will induce uncertainties on photometry.

To correct the measurements on saturated frames, we first used the absolute flux obtained during a clear sky on Montsec, to calibrate the absolute flux measured from Dax, where the cloud absorption was uniform. Next, the corrected absolute flux on Dax was used to calibrate the same fireball moments where Montsec

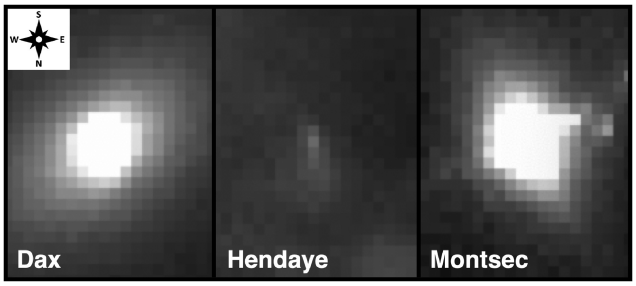

Figure 5. Mosaic of frame region of interest from each station, representing the maximum fireball luminosity time (2018-12-22T21:12:04.837 ± 0.007s UT, depending on the shift in frame acquisition). Image orientation is displayed in the compass rose. The change in PSF is caused by different levels of absorption; Overcast sky on Dax (thin layer) and Hendaye (thick blanket), while Montsec had no clouds in the CCD-fireball line of sight. The white patches for Dax and Montsec are saturated areas.

was saturated. This cross-calibration enhanced the Montsec clipped highlight frames, and allowed to better approximate the radiated energy.

2.2 Airwave evidence

2.2.1 IGN seismic data

The SPMN network obtained additional four distant video recordings of the bolide, and confirmed the seismic detection from four IGN stations (Table 1). The vertical components of the EARA, EALK, ESAC, and ECHI are displayed in Fig. 6, in units of velocity and high-filtered at 1 Hz. The distances between the main ablation location and the stations vary from 50 to 183 km (Fig. 1). The signal is compatible with a sound wave speed propagation and therefore this detection corresponds to the coupled direct wave from the main ablation of the fireball trajectory. Other distant stations of the IGN did not present any signal above the seismic noise background, and given the distribution of the IGN stations (i.e. to the East of the fireball's trajectory), a reconstruction using only seismic methods could not be possible with enough accuracy.

From the amplitudes of the recorded waves, the energy can be estimated using seismic magnitude scales (Kanamori 1977; González 2017). Combining this output with empirical results, the source energy of the impact can be estimated.

2.2.2 IMS infrasound data

The CTBTO (Comprehensive Nuclear-Test-Ban Treaty Organization, Vienna, Austria) operates a network of infrasound stations as part of its IMS. The IMS is a world-wide network that monitors most of the Earth's atmosphere. It was created to find nuclear explosions in the atmosphere on Earth. With the IMS infrasound stations, it is possible to detect the energy released by the impacting meteoroids or asteroids. The network consists of 52 infrasound stations spread around the globe, status as of 2020 May, and upon completion it will contain 60 stations (http://www.ctbto.org). Since it is operational during day and night, it is a unique source for fireball monitoring. The IMS infrasound stations each consist of an array of microbarometer sensors. These sensors are sensitive to frequencies in the range of 0.02–4 Hz (Marty, Ponceau & Dalaudier 2010).

The recorded waveforms were analysed with the program DASE Toolkit - Graphical Progressive Multi-Channel Correlation (DTK-GPMCC), developed in collaboration with the CTBTO by the

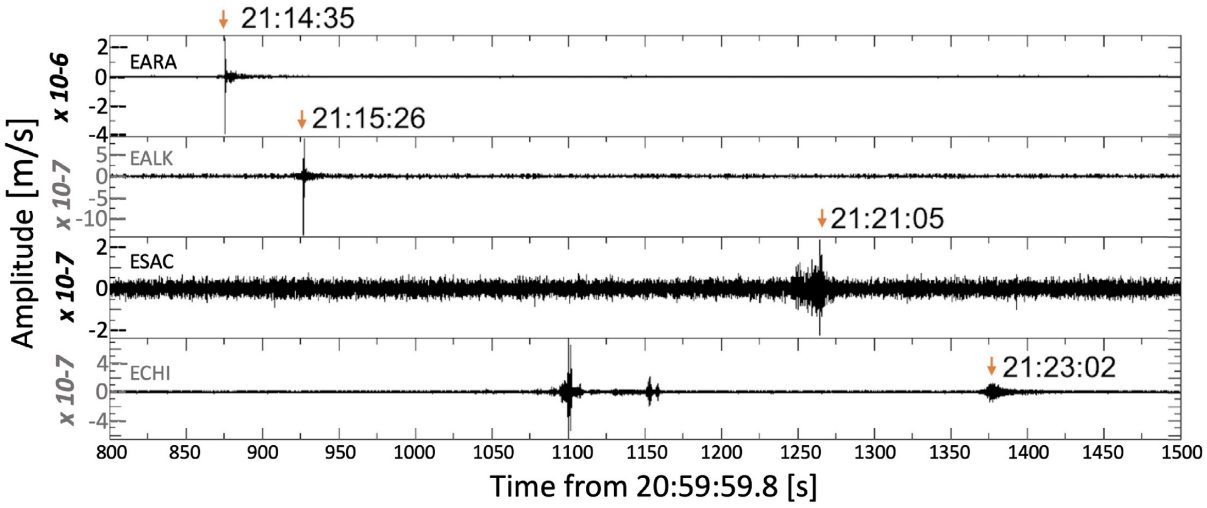

Figure 6. Seismic detection of the fireball from 2018 December 22 at four IGN seismic stations. The recording time for each signal is indicated by the orange arrow. The scale of the seismic plots shows the energy loss due to wave attenuation with distance and the coupling phenomena transforming sound to seismic wave. For further details see the text.

CEA (French Alternative Energies and Atomic Energy Commission, France). The program is based on an algorithm for Progressive Multi-Channel Correlation (PMCC) and detailed by e.g. Mialle & Arora (2018).

For more details about the signal identification the reader is referred to Ott et al. (2019). After the signal was identified its frequency components were used to apply a bandpass filter and to stack the waveforms of the different station's sensors.

There are a variety of methods that aim to determine the energy of the impacting object from infrasound data (Edwards, Brown & Revelle 2006). The empirical methods are based on either the period of a signal, or its amplitude, as described by e.g. Ens et al. (2012). However, the period of the signal seems to be the parameter that is the most stable, i.e. the one that changes the least even during long paths from signal to detection at a station (Edwards et al. 2006). The period is also widely used today. Thus, the period at maximum amplitude of the resultant beam was investigated to compute the source energy. This was done following the method by Revelle (1997).

3 RESULTS

An instrumentally documented fireball (possible meteorite dropper) was observed above the Western Pyrenees on 2018 December 22. The event occurred late in the evening, on $21^{h}12^{m}01\text{-}05^{s}$ ± 0.005 UT (22 h local time). The luminous trajectory started over the south-western part of France, and spent most of the flight time over northern Spain. After a 4.9 s long flight, it terminated over the Navarre region in the northern part of Spain.

During this section, we characterize a range of parameters, from features observed directly, to estimates based on the object's behaviour, aiming to constrain the energy and mass.

3.1 Dynamic data

3.1.1 Trajectory

The longest luminous path of the fireball was seen from Dax, despite the cloud coverage. The detected ablation (between 21:12:00.989 and 12:05.864 UT) corresponds to an 87 km long atmospheric flight along an average slope to the Earth's surface of 36.5°.

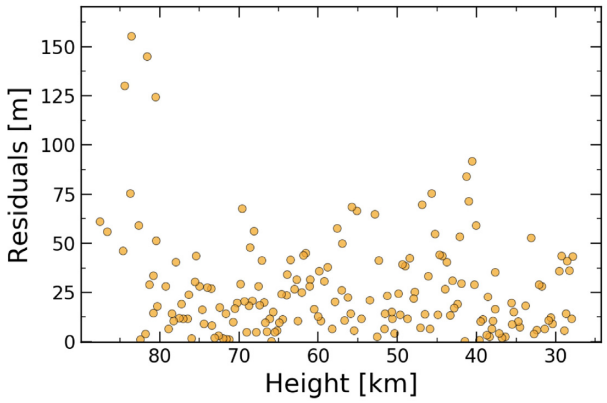

Figure 7. Residual distance along the best computed fireball trajectory. The RMS is 25.9 m, while the median is 19.5.

Montsec was the only station that observed the trajectory unobstructed by clouds. From there, the object started at an elevation of 19.6° and finished at 11.2°, just before the mountain ridge at the horizon. We inspected the recorded *captures* for meteor trains on Montsec as well as on other close cameras, yet no clear train could be identified.

The apparent (instrumental) width along the fireball track, when projected on the distance, varies between 0.5 and 3 km. Nevertheless, the final astrometric measurements allowed a less than 26 m σ for the measured residuals along the trajectory (Fig. 7).

The dynamic parameters are computed based on the rate of body deceleration in the atmosphere. Thus, the altitude and position of the object are fitted according to the analytical model described by Gritsevich (2009), to obtain the entry and final mass of the object. This technique combines two dimensionless parameters: A ballistic coefficient (α) and a mass-loss parameter (β) that interprets how efficient an object moves through the atmosphere. Jeanne et al. (2019) described the implementation of this model for FRIPON.

Results for the trajectory derived from triangulation for all stations are given in Table 2.

Table 2. Geophysical data on the Western Pyrenees fireball.

Initial velocity	24.45 ± 0.12 km s^{-1}	
Final velocity	6.4 ± 0.12 km s^{-1}	
Beginning height	88 km	At Dax all-sky image
Terminal height	27.3 km	At Dax all-sky image
Trajectory length	87 km	
Duration	4.87 s	
Peak absolute magnitude	-12.9 ± 0.7	At the height of 34.4 km
Dynamic pressure at the fragmentation	3.5 MPa	At the height of 34.8 km
Maximum dynamic pressure	4.4 MPa	At the height of 31.7 km
Trajectory slope	36.5°	From horizontal
PE	−3.9	Type I
α	17.307	
β	2.603	
$log(2\alpha\beta)$	1.96	Type I

Table 3. Meteoroid parameters as calculated by FRIPIPE for a range of densities.

ρ_M (kg m^{-3})	Diameter (m)	M_e (kg)	M_f (g)
1500	0.45	71.0	33.5
2500	0.27	25.5	12.1
3500	0.19	13.0	6.2
4500	0.15	7.9	3.7
5500	0.12	5.3	2.5
6500	0.10	3.8	1.8

3.1.2 Density estimation

From the atmospheric trajectory alone, it is rather difficult to estimate the meteoroid parameters. Hence, FRIPIPE also computes a number of scenarios that correspond to several density regimes (Table 3). To further constrain the size of the Pyrenean meteoroid, we analysed multiple accounts where density is discussed in the literature. Also, an estimate of density will be required to calculate the size of the object from photometric and infrasound energy.

Gritsevich & Koschny (2011) note that a meteoroid bulk density range is likely within 1–4 g cm^{-3}. This gap can be narrowed further, in an event of a meteorite recovery. Though often, determining the pre-atmospheric bulk density can be challenging due to the broad diversity in meteoroid size, shape, internal structure, as well as porosity. It is known that large asteroids can have porosities as high as 40–50 per cent (i.e. rubble-piles), and these values are not uncommon for objects at the asteroid-meteoroid border (Hildebrand et al. 2006; Jenniskens et al. 2009). Consolmagno & Britt (1998) conclude that most meteorites are substantially denser than measured density of well-known asteroids. This is not surprising, considering the survivorship bias. Stronger objects will withstand higher pressures along the atmospheric deceleration, and are more likely to reach free fall before vaporizing completely. Moreover, meteorite strength is a poor indicator of parent body bulk strength. Popova et al. (2011) analysed strengths of meteorites along with atmospheric trajectory data, and they estimate a meteorite bulk strength up to two orders of magnitude larger than that of the parent meteoroid (i.e. derived from dynamic pressure, at first fragmentation).

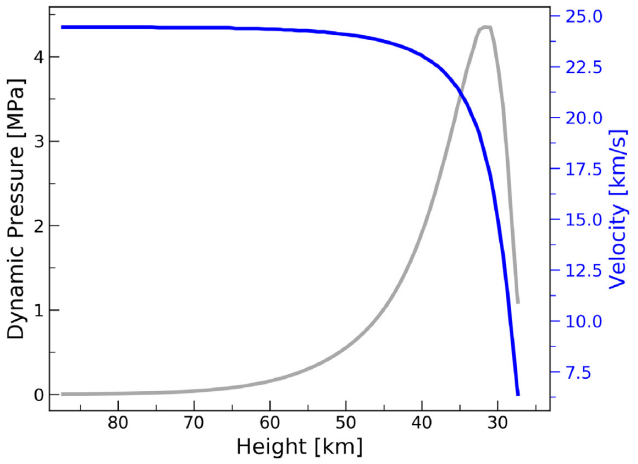

Figure 8. Dynamic pressure experienced by the meteoroid and the velocity fit (blue) are displayed as a function of height.

The overall strength for the Pyrenean meteoroid was measured to be 3.5 MPa at fragmentation, a value quite comparable with other ordinary chondrite fall (Popova et al. 2011). This corresponds to the dynamic pressure (Fig. 8) experienced by the object as:

$$p = \rho_h \, v_h^2, \tag{1}$$

where v_h is the velocity and ρ_h is the atmospheric density modelled at the height of the disruption event (depicted in Fig. 9, frame #1). The units for ρ are g cm^{-3}, obtained from *NRLMSISE-00* model (Picone et al. 2002).

Following Register, Mathias & Wheeler (2017), this overall strength is not representative for any specific material property of the meteoroid such as compressive strength, tensile or yield strength. This measurement rather acts as an aggregate strength, encompassing all of the above. Moreover, meteoroid durability may change depending on its size. Usually, larger objects are more likely to contain faults and cracks in their volume, which lowers their strength. A smaller object having the same density can undergo larger ram pressures before fragmentation, thus reaching a lower end height. Work on this regard was carried out e.g. based on the data collected in the Praerie Network (PN).

By analysing around 200 PN fireballs (ranging from ≈cm to sub-meter in diameter), Ceplecha & McCrosky (1976) noted that meteoroids having similar masses reached rather different end heights. These were interpreted as strength differences, and they proposed a 1D criterion, termed PE (from ρ_E, the atmospheric density at the end of the luminous trajectory) which can be used to associate the overall strength, with one of four groups (i.e. ordinary chondrite-like, carbonaceous chondrite, short-period cometary, and weak cometary material). The original relation which was widely used ever since is given by:

$$PE = log(\rho_E) + log(M_e)A + log(V_\infty)B + log(cos\ Z_R)C, \tag{2}$$

where M_e is the entry mass in kg, V_∞ is the entry speed in km s^{-1}, Z_R is the zenithal angle of the radiant and a set of constants, derived empirically as: $A = -0.42$, $B = 1.49$, $C = -1.29$.

For the Pyrenean fireball, we computed the PE criterion with respect to the previous entry mass estimations (Table 4). All the values fit into the Type I category, which is associated with ordinary

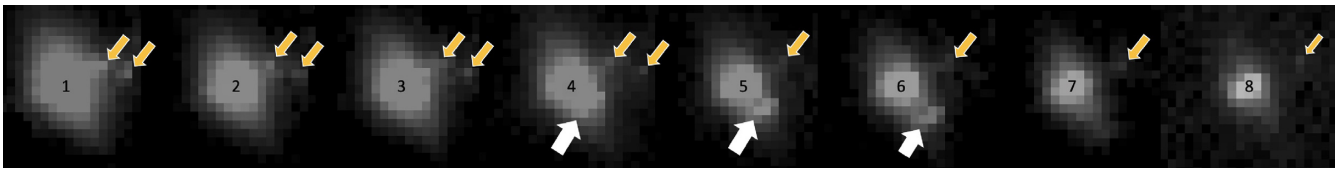

Figure 9. Mosaic of fireball frames as seen from Montsec station. Time flows from left to right, first frame corresponding to the point of maximum luminosity. The yellow arrows indicate fragments detached before the explosion. Closely after the main disruption (#1), a secondary fragmentation occurs during frame #3. This briefly increased the luminosity of the object, and can be seen in a second peak in Montsec light curve (Fig. 10). The fragment (white arrow) is left behind the main body in the following three frames.

Table 4. PE criterion of the fireball for the range of entry masses obtained in Table 3.

M_e(kg)	71.0	25.5	13	7.9	5.3	3.8
PE	−4.25	−4.06	−3.94	−3.85	−3.78	−3.71

chondritic material. This Type I has been studied extensively, as most of the recorded meteorite falls, match this category.

Another estimator of strength was recently proposed by Moreno-Ibáñez et al. (2020) as an alternative to the PE criterion. It combines the before-mentioned dimensionless parameters as $2\alpha\beta$, and by taking their logarithm, the authors rendered a new method of classification, which does not involve empirical constants. In this manner, we obtain a $log(2\alpha\beta)$ of 1.96, which corresponds again, to a Type I fireball class.

From the conclusions mentioned above, along with the meteoroid single-body behaviour until the last second (Section 3.2), we expect that a density of 3.5 g cm^{-3} (characteristic to ordinary chondrites), would be optimal for modelling the mass and energy of the Pyrenean fireball (Table 7).

3.2 The light curve

To obtain the light curve of the fireball, we applied the steps detailed in Section 2.1.2, and plotted the absolute magnitude as a function of time and height (Fig. 10).

Both the Hendaye and Dax cameras recorded the event through a layer of clouds, producing absorption and reflectance of light by the water/ice particles. For thin clouds, a part of radiation was attenuated along the path between the source and detector. Another part was scattered by clouds back into the detector. As the cloud layer increased, the total detected light was dominated by re-scattered light. When the fireball PSF is summed for each frame of the detection, it will result in an apparent decrease of meteor radiation, thus explaining the apparent final drop in brightness as seen from Hendaye, starting from a height of approximately 37 km.

The saturation correction routine is applied by enhancing the clear sky light curve from Montsec, based on a selection of frames from the Dax station, where cloud filtering was uniform (see Section 2.1.2). The shaded area surrounding the model represents the error bar. This combines the errors involved throughout the measuring process (i.e. flux, background, extinction, and saturation correction). The beginning and the end of the light curve error is significantly wider (≈ 1 mag) due to Poisson error, on low flux count. One second into the ablation, the uncertainty due to saturation corrections begins to dominate.

The fireball light curve is unusually flat for an entry with a velocity of 24 km s^{-1}. Small detaching fragments have been spotted on individual frames late in the ablation (Fig. 9), yet they were not associated with a particular increase in luminosity in the light curve.

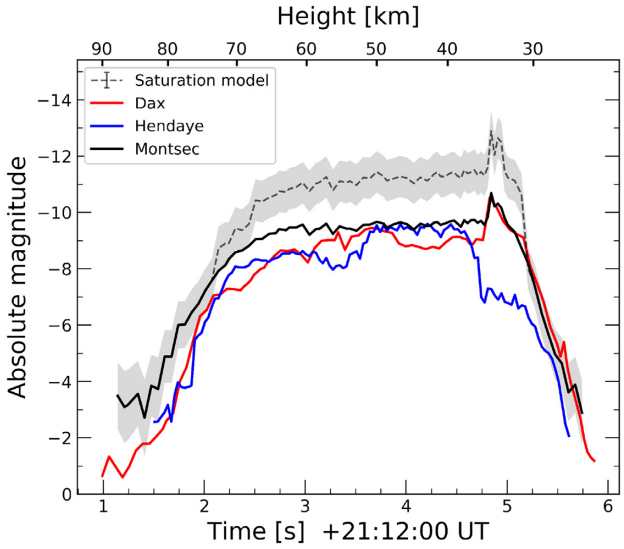

Figure 10. The fireball light curve as seen from each station in units of absolute magnitude (i.e. normalized to 100 km). Height is computed from the trajectory as a function of time and displayed in the upper axis. The input used to obtain the saturation correction along with the uncertainty on values (shaded area) are detailed in Section 3.2.

This behaviour is congruent with a distinct object of higher bulk strength, with some prominences that were detached at dynamic pressures of 1 MPa, well before the disruption event, which occurred at 3.5 MPa.

Similar behaviour was observed on larger objects. Borovička et al. (2020) indicate two strengths that may appear in the light curve of sub-meter to meter scale ordinary chondrites. The first consists of the shedding phase, where the meteoroid loses its weak material on the surface which can be seen as a peak at very low ram pressures (between 0.04 and 0.12 MPa), and a second strength, that conveys the meteoroid internal solidity which is usually catastrophic for the object. A distinct signature of first strength was not observed for the Pyrenean fireball, which could be due to the limitation in measurement resolution, or simply the meteoroid did not hold any frail surface structures. The second strength is the disruption of the object at the height of 34.4 km that also corresponds to the point of maximum brightness of −12.9 ± 0.7 mag. This was recorded on both the Montsec and Dax stations as a brief single-frame flash at 21:12:04.836 ± 0.007 UT, and was followed by a weaker flash (two frames later). This is interpreted to be a second fragmentation, which due to clouds, could only be observed from Montsec. Right after, the object slowed down to a third of its initial velocity, and ablation could only be maintained for less than a second.

Table 5. Seismic energy equivalence.

Station code	Max amplitude ($\mu m\,s^{-1}$)	M_{IGN}	$E_{seismic}$ (kt)
EARA	3.9	2.5	8.6^{-5}
EALK	1.3	2.3	3.7^{-5}

One method of obtaining the object's mass is by integrating the radiated energy. Thus, the source energy is estimated from the photometry following the manner described by Brown et al. (2002), and by plugging the entry velocity into $m = \frac{E}{0.5\,v^2}$ we obtain the entry mass. For this, the corrected light curve magnitude (M) was converted into energetic units assuming a plasma temperature of 4500 K emitting in the whole spectrum (Ceplecha et al. 1998) as others have used when converting bolide magnitudes (e.g. Ceplecha 1996; Spurný et al. 2010). The relation can be arranged to obtain I in Watts as:

$$I = I_0\ 10^{\left(\frac{M}{-2.5}\right)} \tag{3}$$

where I_0 is estimated to 1500 W and represents the intensity of a 0 magnitude light source. Thus, by integrating along the fireball's duration, a total radiated energy (E_o) of 1.3×10^8 J was found, which is equivalent to 3.18×10^{-5} kt TNT. This value will be further used in Section 4 to estimate the source energy by comparing it with well-known bolides (Table 6).

3.3 Airwave energy

3.3.1 Seismic

On two of the IGN stations (EARA and EALK) situated at 50 and 72 km from the bolide blast, the seismic signal formed a typical N shape, and was associated with the direct wave created by the main disruption of the meteoroid (Section B). Both stations display the precursor surface waves and the direct coupling. In addition, the signal from EARA station, also shows the mixed direct coupled waves with surface seismic waves. These features are presented in detail in Fig. B1.

To minimize the attenuation effects due to larger distances, only the signals recorded at the nearest seismic stations from the trajectory (i.e. EARA and EALK), were kept for energy estimation. Thus, the IGN seismic magnitude is computed (M_{IGN}, with the scale fitted to the Spanish seismic network), and by using the empirical magnitude-to-energy conversion from Kanamori (1977), a seismic source energy ($E_{seismic}$) was estimated. The results for both stations are displayed in Table 5.

To translate $E_{seismic}$ into a kinetic energy of the object, an acoustic efficiency correction is needed. This is based on the assumption that the ground motion (detected by seismographs) is caused by direct loading of the surface by acoustic overpressure generated by the meteoroid. This was described by e.g. Edwards et al. (2007), and the references therein. Upon evaluating the US Air Force Technical Applications Centre (AFTAC) detected atmospheric impacts, ReVelle & Whitaker (1996) obtained acoustic efficiencies ranging from 0.2 to 7 per cent, with larger efficiencies corresponding (on average) to smaller objects. This is in agreement with acoustic efficiencies obtained by Ens et al. (2012), where the authors report a variation in acoustic efficiency of several orders of magnitude (0.1 to 20 per cent). Thus, emphasizing the individual nature of each event. Converting the mean $E_{seismic}$ (between EARA and EALK), according to the range of acoustic efficiencies obtained by ReVelle & Whitaker (1996), would place the Pyrenean meteoroid kinetic energy between 0.001 and 0.03 kt TNT. These margins, along with the corresponding meteoroid parameters are presented in Table 7.

3.3.2 Infrasound

Despite the small size of the object entering the Earth's atmosphere on 2018 December 22 it was detected by an IMS infrasound station. The station I48TN is located in Tunisia and recorded a quite clear signal of the event. It is displayed in Fig. 11. The station had an estimated distance of roughly 1265 km to the event. Taking the traveltime of the acoustic wave through the atmosphere into account the displayed signal detected around 22:20 UT arrived as expected. Furthermore, the median of the back azimuths of the identified signal of 315.6° is as expected. The back azimuth of the wave is given in degrees as seen from the station. It is the direction the signal arrives from. In the figure different parts of the signal can be seen which result from multiple wave packages arriving at the station. Due to different paths through the atmosphere the traveltime of the wave packages varies. For more detailed information about atmospheric propagation modelling, see e.g. Pilger et al. (2020).

We found values for the period at maximum amplitude of $P = 3.8$ s and $E_{infrasound} = 0.45$ kt TNT equivalent for the source energy. Combining this with the velocity computed from the FRIPON data of $v_{infrasound} = 24.45\ km\,s^{-1}$, which is more robust to oversaturation allows a mass estimation for the entering object of about $m_{infrasound} = 6.3$ t. Assuming a density of $\rho = 3500\ kg\,m^{-3}$, this would correspond to an entering asteroid with a diameter of about $s_{infrasound} = 1.5$ m. It has to be mentioned that I48TN was the only IMS infrasound station in which a signature of the fireball could be identified. This leads to larger uncertainties of the results.

Since the infrasound station in Germany, I26DE, had a similar distance to the fireball (about 1350 km), we also investigated its data for a signature of the fireball. Unfortunately, we could not find any significant detection. This is surprising, since both directions (from the fireball to I48TN and I26DE) and distances are well suited for wave propagation. This indicates better observation conditions at the Tunisian station compared to the German one.

4 COMPARISON BETWEEN ENERGY ESTIMATES

A direct formula between the kinetic energy of the impactor, and the light generated in the atmosphere has so far not been found. It must be a complex function that encompasses the parameters of the object (e.g. composition, density, mass, shape, structure, etc.), the impact geometry, as well as the behaviour of the air particles during the deceleration. Most of these parameters remain unknown to us.

Early studies used theory or independent methods in an attempt to measure how efficient the light production is during the atmospheric interaction. Brown et al. (2002) estimated this ratio using an empirical fit between the observed radiation and energy derived through various techniques. The original relation was presented as:

$$\tau = (0.1212 \pm 0.0043)\ E_o^{0.115 \pm 0.075}, \tag{4}$$

where E_o is passed in kt and τ is the ratio of kinetic energy which can be attributed to radiated light, also known as the luminous efficiency.

For the fireball radiated energy rank, the uncertainty in equation (4) translates into a variation in τ between 1.7 and 8 per cent, while the fit

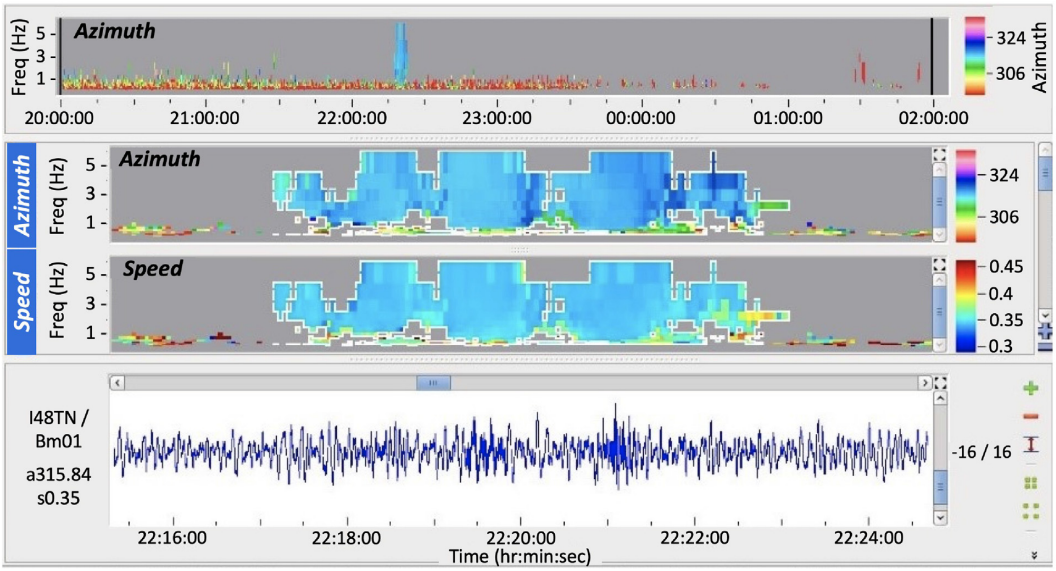

Figure 11. Infrasound signal of the fireball from 2018 December 22 recorded by IMS station I48TN in Tunisia processed with PMCC. On the top, the result of PMCC is presented for the whole investigated time period from 20:00 UT on 2018 December 22 until 02:00 UT on 2018 December 23. The different wave directions (back azimuths) are colour coded. The middle shows an enlarged part with time frame ranging from about 22:16 UT until 22:24 UT. For the analysed frequency bands, the computed back azimuth and the velocity of the recorded infrasound signal are shown. At the bottom for the same time interval the resultant beam is presented.

results in 3.7 per cent. We found that for a single-body behaviour the margins are in agreement with other estimates of luminous efficiency (e.g. Ceplecha et al. 1998; Gritsevich & Koschny 2011). However, the optical energy emitted by the Pyrenean meteoroid places the object outside the interval of measurements proposed by Brown et al. (2002).

To better understand the radiated light – source energy relation, a set of well-studied events were selected, which displayed similar optical energy to the meteoroid in this study. From the objects with published data, which were subject of meteorite recoveries and have well-studied trajectory (including calibrated light curve), 11 correspond to the energy ranging from 0.1 to 10 ton TNT. To this group, we added a few fast, high altitude bolides detected via multiple instruments, including close proximity infrasound and fast radiometers, which allowed a precise estimation of the source energy. The full set of objects along with their physical details are presented in Table 6. When fitting the full set of objects from Table 6 as source energy versus optical energy, we obtain the best-fitting relation:

$$log(E) = 0.7165\ log(E_o) + (0.5932 \pm 0.5020), \quad (5)$$

where E represents the impact energy. A visual representation of this energy correspondence is displayed by the red line in Fig. 12. This is an extension for the relation proposed by Brown et al. (2002), obtained for impacts displaying lower energies. By applying this relation on the Pyrenean meteoroid yields a total energy of 1.1 tons TNT equivalent. The corresponding photometric mass was estimated to be 15 kg, which in turn, given a density of 3500 kg m^{-3} and a spherical shape, leads to a diameter of 0.2 m. This result is higher compared to the mass of ≈12 kg obtained using the method proposed by Brown et al. (2002). This is not surprising, considering that the latter was derived from more energetic events (0.1–1 kt TNT-scale). Moreover, the empirical relation presented in this work (equation 5) is bridging the gap towards lower mass objects, which were found to be even less efficient in radiating light (e.g. Subasinghe, Campbell-Brown & Stokan 2017, and the references therein). These results along with estimates from other methods are listed in Table 7.

Though objects the size of the Pyrenean meteoroid impact the Earth on a daily basis (Brown et al. 2002), there are hardly any studies that discuss the instrumentally combined data of decimeter-size objects. Upon analysing events recorded by the FRIPON network, the object presented here was the only one found to generate a strong enough infrasound signal to be detected by IMS stations. Similar source-to-detector geometry displayed the Bunburra Rockhole meteoroid. However, after extensive searches, Spurný et al. (2012) reported that there were no infrasound signals recorded for the event. This indicates the fact that atmospheric conditions are quite important for signal propagation. The Pyrenean fireball energy resulted from the infrasound estimate (0.45 kt TNT), is several orders of magnitude larger than the photometric estimate. This is not surprising, since the AFTAC relation was obtained measuring highly energetic nuclear explosions. Previous authors have shown that the energy estimations using this method are less reliable for energies below 0.2 kt, and larger than 10 kt (Edwards et al. 2006). For Chelyabinsk impactor, Ott et al. (2019) found energy estimates which vary by several orders of magnitude. When the authors considered the mean of the observed period, the results agree favourably with other energy estimates, thus marking the importance of infrasound networks.

Among the energy signature observed and the proposed equivalence presented in the literature for each method, we found that the integration of the emitted light presents the lowest uncertainty around the ton TNT-class impacts (Fig. 13). This was indicated also by the nominal value of the dynamic mass for the estimated density. The large error on dynamic mass is the theoretical standard deviation due to possible uncertainties such as the 'shape factor' and the fragmentation during flight. In our case, we already know the fragmentation did not occur until the very end, which we consider the nominal value to be the most likely mass. A larger uncertainty is indicated by the seismic and infrasound estimates. Hence, we retain the approximate value of 1 ton TNT as a final energy estimate, which

Table 6. Details of the calibrated bolides used. The table lists (from left to right) the name of the meteorite linked with the fireball (or the fireball name as given in the source study), date of impact, the pre-atmospheric velocity and mass, the maximum luminosity reached (in magnitudes), the optical and the impact energy in tons of TNT (1 T $= 4.184 \times 10^9$ J), and the references for the data.

Bolide name	Date (yyyy/mm/dd)	V_∞ (km s^{-1})	m_∞ (kg)	M_{max}	Optical energy (T TNT)	Source energy [b] (T TNT)	Reference
Hamburg	2018/01/17	15.83 ± 0.05	142 (60–225)	−16.3	0.193 [a]	4.27 (1.79–6.78)	1, 2
Ejby	2016/02/06	14.52 ± 0.10	185 (110–350)	−14.0	0.156 [a]	4.66 (2.73–8.94)	3, 4
Creston	2015/10/24	16.00 ± 0.26	55 (10–100)	−12.0	0.040 [a]	1.68 (0.30–3.16)	5
Žďár nad Sázavou	2014/12/09	21.89 ± 0.02	150 (130–170)	−15.3	0.335	8.59 (7.43–9.75)	6
Novato	2012/10/18	13.67 ± 0.12	80 (45–115)	−13.8	0.215	1.79 (0.99–2.61)	7
Križevci	2011/02/04	18.21 ± 0.07	50 (25–100)	−13.7	0.064 [a]	1.98 (0.98–3.99)	8
Grimsby	2009/09/26	20.91 ± 0.19	30 (20–50)	−14.8	0.082 [a]	1.57 (1.03–2.66)	9
Jesenice	2009/04/09	13.78 ± 0.25	170 (90–250)	−15.0	0.158 [a]	3.86 (1.97–5.88)	10, 11, 12
Bunburra Rockhole	2007/07/20	13.37 ± 0.01	30 (21–38)	−9.6	0.004 [a]	0.64 (0.44–0.82)	13, 14, 15
EN130801	2001/08/13	59.89 ± 0.13	0.600	−13.3	0.006	0.257	16
EN151101A	2001/11/15	71.30 ± 0.11	0.800	−14.9	0.029	0.486	16
EN030804	2004/08/03	60.80 ± 0.20	0.370	−12.5	0.005	0.163	16
Innisfree	1977/02/06	14.70 ± 0.04	36 (20–44)	−12.1	0.040	0.93 (0.51–1.14)	17, 18
Lost City	1970/01/04	14.14 ± 0.01	163 (158–168)	−12.4	0.065 [a]	3.90 (3.78–4.02)	18, 19

Notes: The foremost value for both the entry mass (m_∞) and source energy represents the preferred estimate from the references. The ranges in the parentheses cumulate the uncertainty intervals presented in the references. [a] The optical energy was extracted via digitization from the calibrated light-curve plot in the reference, when the study did not present the integration value of the radiated light. For details about the extraction method, the reader is referred to Anghel & Birlan (2017). [b] The source energy was computed from references as $E = 0.5\, m_\infty V_\infty^2$.
References: [1] Brown et al. (2019); [2] Heck et al. (2020); [3] Spurný et al. (2017); [4] Haack et al. (2019); [5] Jenniskens et al. (2019); [6] Spurný et al. (2020); [7] Jenniskens et al. (2014); [8] Borovička et al. (2015a); [9] Brown et al. (2011); [10] Spurný et al. (2010); [11] Bischoff et al. (2011); [12] Ott et al. (2010); [13] Sansom et al. (2015); [14] Spurný et al. (2012); [15] Welten et al. (2012); [16] Brown et al. (2007); [17] Halliday, Griffin & Blackwell (1981); [18] Ceplecha & Revelle (2005); [19] Ceplecha (1996).

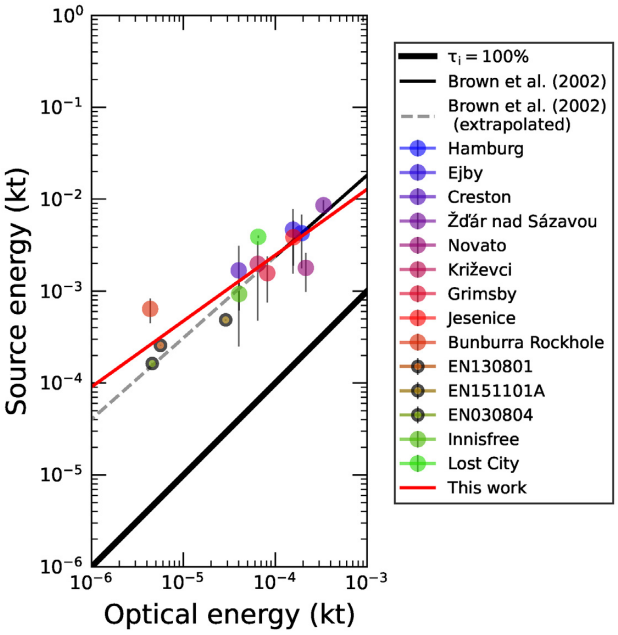

Figure 12. Energy calibrations of well-known bolides around the ton-scale TNT. The error bar on the source energy represents the combined uncertainties from mass and velocity. The thin black line is the fit obtained by Brown et al. (2002) corresponding to source energies greater than 0.1 kt TNT. This is continued with the dotted grey line on to this energy category. The red line is obtained as a best fit of the calibrated impact energy from Table 6. The displayed objects have well-studied trajectory data, and all except the small circles with black contour were the subject of successful meteorite recovery campaigns. The 100 per cent luminous efficiency correspondence is represented by the thick line.

corresponds to the nominal value overlap of the results obtained through photometric and dynamic methods. This translates into an acoustic-seismic efficiency of ≈ 7 per cent, which is in agreement with previous work, and could be explained by the high overall strength, and single body ablation.

5 DISCUSSION

The 2018 December 22 fireball brought attention of multiple casual witnesses throughout southern France (despite the cloud coverage), and all over Spain.

Among the 29 detailed descriptions on IMO website (event 5756-2018), the majority (23) reported green being the dominating colour during the luminous path, followed by yellow, orange, and red. The video footage recorded by a camera installed at Calar Alto Astronomical Observatory (Spain), 600 km from the fireball path confirmed the colours reported by eyewitnesses (Yanguas et al. 2019). Even so, the fireball colour is a poor indicator of meteoroid composition. However, when spectroscopic observations are available, one can distinguish between achondrites, chondrites, and metallic material (e.g. Borovička, Spurný & Brown 2015b; Drouard et al. 2018).

FRIPON network contains radio antennas which are tracking radio signals emitted by Graves, the French radio transmitter (Rault et al. 2018; Colas et al. 2020). Head and trail echos related to meteors are recorded into FRIPON database. No radio echo related to this event was recorded.

The reported luminosity of the fireball in stellar magnitude is −13 (i.e. median value, from all visual observers), surprisingly confirmed by the corrected light curve (see Section 3.2), considering the usual overestimation in declared brightness amid eyewitnesses.

Among multi-instrument recorded bolides, the Pyrenean fireball had a fairly low energy. This is based upon dynamic and photometric

Table 7. Summary of results for source energy, mass, and equivalent diameter of the Western Pyrenees meteoroid derived from different methods.

Technique	Estimated energy [J]	Estimated energy [kt]	Initial mass [kg]	Equivalent diameter [m]
Dynamic model	4 (0.12–7.8) × 10^9	1 (0.03–1.9) × 10^{-3}	13 (0.4–26)	0.2 (0.01–0.4)
Radiation[a]	3.6 (1.6–8.1) × 10^9	0.9 (0.4–1.95) × 10^{-3}	12 (5–27)	0.2 (0.14–0.25)
Radiation[b]	4.5 (2.7–7.5) × 10^9	1.1 (0.7–1.79) × 10^{-3}	15 (9–25)	0.2 (0.17–0.24)
Seismic energy	3.7 × 10^9–1.3 × 10^{11}	1 × 10^{-3}–0.03	12–430	0.2–0.6
Infrasound energy	1.9 × 10^{12}	0.45	6300	1.5

Note: [a]Results obtained based on equation (4). [b]The source energy resulted via an optical correspondence based on equation (5). The foremost value of each section represents the best estimate for the range enclosed in parentheses (if present). Dynamic energy was computed from an initial velocity of 24.454 km s^{-1} (see Table 2). The equivalent diameter for the pre-atmospheric body assumes the object is a sphere, with a bulk density of 3500 kg m^{-3}.

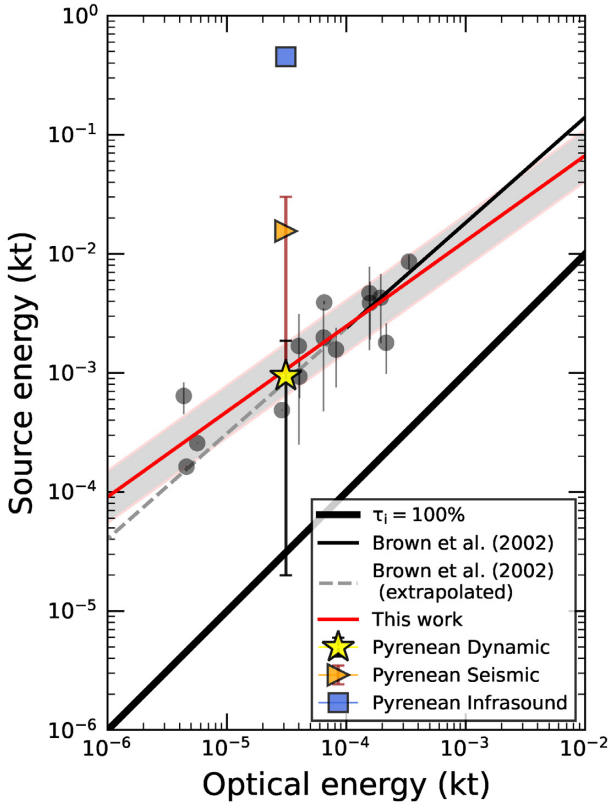

Figure 13. Energy calibrations of well-known bolides around the ton-scale TNT. For further details about the background data, see Fig. 12. The Pyrenean impact energy is displayed as the result of dynamic, seismic, and infrasound methods along with associated uncertainties. The best fit uncertainty (grey area) represents the standard deviation of the calibrated bolides.

mass estimations. Although there are large uncertainties for these methods, both agree on the order of magnitude for the nominal energy (Table 7), giving an estimate of ≈1 ton TNT. Though the uncertainties of radiation-based estimations are discussed extensively by various authors, we considered the optical based energy estimation favourable for the fireball presented here. This is due to the quasi-continuous ablation character until the very end of the light curve. In different circumstances, a heavy fragmenting object would need a more attentive approach when applying luminous efficiency, as the object's luminosity can be increased by small detaching fragments which burn faster and using the integral efficiency model can overestimate the final energy. This caused a large gap between dynamic and photometric mass, as presented by e.g. Borovička et al. (2015b).

For the meteor presented in this study, the average infrasound period at maximum amplitude yields an energy of 0.45 kt TNT. Though the infrasound SNR was quite high, a single station record (I48TN) makes it difficult to infer the uncertainty caused by the atmosphere. Hence, we expect that the dynamic and photometric energy of 1 ton TNT (Table 7) to be a better estimate of the object's true parameters. For a detailed discussion of the uncertainties of the evaluation and methods of meteor generated infrasound and possible reasons, we refer to Ott et al. (2019).

In view of the most likely energy estimate (1 ton TNT), the acoustic efficiency obtained from seismic measurements would be 7 per cent; slightly higher than acoustic-seismic coupling efficiency measured by Edwards et al. (2007), while matching the upper limit obtained by ReVelle & Whitaker (1996). Also, this would be significantly lower than the values reported for objects with highest acoustic efficiency presented by e.g. Ens et al. (2012), which could still be applicable to the Pyrenean meteoroid (though unlikely), considering that even a smaller mass is allowed by the lower boundary of the photometric and dynamic estimates (Table 7).

The single body behaviour until the very end, as seen from the quasi-flat light curve, reveals the behaviour of a strong object, which brought its energy low in the atmosphere, being congruent with a high air-to-ground efficiency. This can also be explained by the strong coupling of the airwave to the Earth's surface at the seismic stations near the trajectory, followed by a rapid attenuation of the airwave, as seen in Fig. 6. Such behaviour is consistent with the entry of a small object, which generates a narrow blast cylinder, thus attenuating the shock more rapidly, as apposed to a gross fragmentation generated shock.

This Pyrenean fireball was one of many objects that reached the maximum sensibility limit of our cameras. Circumstances as such, could also lead to the dimming of several low intensity phenomena (e.g. sparks, small flares, rotational features, etc.), that would otherwise convey important elements of the meteoroid. Here, a calibrated radiometer would pinpoint distinct features in the light curve (Rault & Colas 2019), which provide additional information that could be linked with parent bodies.

In order to explore the dynamical history of the meteoroid, we performed a back numerical integration for the last 200 kyears. A set of 2300 clones was created using a Gaussian distribution on the six orbital elements starting from their mean and σ values as provided by FRIPIPE (Table 8). The clones were integrated in the framework of a dynamical model of the Solar system, which includes all the planets

Table 8. Fireball radiant and heliocentric orbit.

Apparent radiant (J2000.0)		
Right ascension	159.18°	
Declination	75.87°	
V_∞	24.454	± 0.118 km s^{-1}
Orbital elements (J2000.0)		
Perifocal distance	0.7906	$\pm$ 0.0024 au
Eccentricity	0.328	$\pm$ 0.011
Inclination	37.3597°	$\pm$ 0.13°
Ascending node	270.712°	$\pm$ 0.0004°
Argument of periapsis	258.174°	$\pm$ 1.773°
Mean anomaly at epoch	313.133°	$\pm$ 2.486°
Semi-major axis	1.176	$\pm$ 0.023 au
Epoch	18 Dec 2018	21:14 $\pm$ 4.5 h

Note. Uncertainties represent 1σ.

along with Pluto, Ceres, Pallas, and Vesta as perturbing bodies. The Earth and the Moon were treated as separate bodies. The model also accounts for the Sun's general relativity contribution (Nedelcu et al. 2014).

The nominal orbit shows an object at relatively high inclination (i), with perihelion near Venus orbit, aphelion in between Earth and Mars (Fig. C2), and moderate eccentricity (e). The clones cloud splits early during the integration, due to close approaches with the Earth (Fig. C1). Although the evolution is strongly chaotic, with a Lyapunov time of only 30 yr, typical for NEO (Tancredi, Motta & Froeschlé 2000), only 18 clones (0.8 per cent of the total) were removed by Earth impacts during the 200 kyears numerical integration.

The clones evolution is confined in a relatively narrow region, with a semimajor axis (a) between 1.1 and 1.25 au, and an eccentricity between 0.03 and 0.39 (Fig. C3). The average residence time of the clones was computed using bins for a and e of width 0.0004 au and 0.0144, respectively. This residence time map can then be used to infer the past dynamical history of the meteoroid, and its most probable source of origin. Most of the clones reside at low (0.05) and high (0.33) eccentricities, with a lower density in the transitional region between these values. This behaviour is suggestive for Kozai–Lidov secular resonance (Kozai 1962), which generates large amplitude anticorrelated oscillations of e and i, with the argument of perihelion (ω) locked or librating (Michel & Thomas 1996). This can be observed in Fig. C1, where a large population of clones undergo this type of inclination and eccentricity oscillations. The typical evolution of a clone in Kozai–Lidov resonances is presented in Fig. C4. For this clone, ω is librating around 270° between -30 and -160 kyears and slowly circulating otherwise. We note that the libration centre is close to the nominal value $\omega = 258.174°$. This configuration provides a protection mechanism from planetary close approaches, since at $\omega = 270°$ and large inclination, the apsides are situated outside the ecliptic plane (Michel & Thomas 1996). Thus, despite orbiting the inner Solar system region, the Western Pyrenees meteoroid appears to be in a relatively stable, *protected* orbital configuration, and, most probably a long time survivor of its precursor body.

6 SUMMARY AND CONCLUSIONS

We report an extensive analysis of the instrumentally detected fireball which occurred on 2018 December 22 at 21:12:01-06 UT and the results obtained when analysing the energy signature of events of this scale.

During flight, the Pyrenean meteoroid displayed a fairly high overall strength, as it underwent relatively large dynamic pressures before the fragmentation event. Though we are not aware of any meteorite findings, we found that a meteoroid density of 3.5 g cm^{-3} is most probable. This value was used to estimate the dynamic mass, which corresponds to a kinetic energy of ≈1 ton TNT.

A second method to estimate the energy was through photometry. The corrected radiated light was attained after the application of a saturation model, as the fireball's luminosity exceeded the ADU limit of our cameras. This resulted in a maximum magnitude (at fragmentation) of -12.9 ± 0.7.

To find a connection between the object's optical integrated energy and the impact energy, a set of well-studied events with similar energy signatures were analysed. From this, an empirical relation was derived, and the resulted impact energy is attributed to an approximate value of 1 ton of TNT. We show that this empirical relation presents the lowest uncertainty in energy measurement among the methods explored in this study. Moreover, the photometric mass proposed by this relation agrees remarkably well with the nominal dynamic mass obtained for the inferred density. This indicates the possibility of future fireball studies based on the radiated light and the dynamic model, to further pinpoint the meteoroid density in addition to the usual mass estimations.

The infrasound period at maximum amplitude yielded an energy estimate of 0.45 kt TNT. This introduced a discrepancy of >2 orders of magnitude between estimates. Though the source signal was detected with a quite high SNR at the IS48TN station, we highlight some inaccuracies for infrasound results, especially since the event was only detected with one station.

As a last step, we explored the dynamical history of the Pyrenean meteoroid through back integrations. Thus, the object was found to occupy a somewhat protected torus, which indicates that it might be long survivor of its parent body. We expect that other objects confined in a similar protected orbital configuration to intersect Earth's orbit.

The empirical relation presented here reveals the robustness of photometric-derived energy measurements of ton TNT-scale impacts, which in turn can enhance the empirical acoustic-based relations at the limit of experimental data. This becomes important for improving the existing measurements of meteoroid flux density, especially now, within the big data context, generated by an increasing size and number of fireball networks.

ACKNOWLEDGEMENTS

FRIPON is funded by the ANR grant N.13-BS05-0009-03, carried by the *Paris Observatory, Muséum National d'Histoire Naturelle, Paris Sud University and Institut Pythéas (LAM-CEREGE)*. Vigie-Ciel is part of the *65 Millions d'Observateurs* project, carried by the *Muséum National d'Histoire Naturelle*, funded by the French *Investissements d'Avenir* program. FRIPON data are hosted and process at Institut Pythéas SIP (Service Informatique Pythéas), a mirror is also installed at IMCCE (Institut de Mécanique Céleste et de Calcul des Éphémérides/Paris Observatory) with the help of IDOC[2] (Integrated Data and Operation Center) supported by CNRS ans CNES. The seismic data were provided by the Instituto Geográfico Nacional (IGN), Spain. S. Anghel and D. A. Nedelcu were supported by a grant of the Romanian Ministry of Research

[2]https://matplotlib.org/basemap/

and Innovation, CCCDI - UEFISCDI, project number PN-III-P1-1.2-PCCDI-2017-0226/16PCCDI/2018, within PNCDI III. EP-A and JMT-R acknowledge funding from PGC2018-097374-B-I00 (MCI-AEI-FEDER, EU). M. Birlan work was partly supported by SEEING-IEA CNRS program. R. Hueso and A. Sánchez-Lavega were supported by Diputación Foral de Bizkaia and Gobierto Vasco IT1366-19. Fig. 1 was built using data from NASA Worldview, copyrighted according to National Aeronautics and Space Administration Open Source Software Agreement Version 1.3. We thank M. Gritsevich for comments and suggestions that helped improve the earlier version of this manuscript.

DATA AVAILABILITY

The data underlying this article are available in the article and in its online supplementary material, under the name (*Pyrenean_trajectory.csv*).

REFERENCES

Anghel S., Birlan M., 2017, Rom. Astron. J., 27, 3
Anghel S., Birlan M., Nedelcu D. A., Boaca I., 2019, Rom. Astron. J., 29, 189
Audureau Y. et al., 2014, in Rault J. L., Roggemans P., eds, Proceedings of the International Meteor Conference. The International Meteor Organization, IMC 2014, Giron, France, p. 39
Bischoff A. et al., 2011, Meteorit. Planet. Sci., 46, 793
Borovička J., 1990, Bull. Astron. Inst. Czech., 41, 391
Borovička J. et al., 2015a, Meteorit. Planet. Sci., 50, 1244
Borovička J., Spurný P., Brown P., 2015b, Small Near-Earth Asteroids as a Source of Meteorites. The University of Arizona Press, Tucson, p. 257
Borovička J., Spurný P., Shrbený L., 2020, AJ, 160, 42
Brown P., Spalding R. E., ReVelle D. O., Tagliaferri E., Worden S. P., 2002, Nature, 420, 294
Brown P. G., Edwards W. N., Revelle D. O., Spurny P., 2007, J. Atmos. Sol.-Terr. Phys., 69, 600
Brown P. et al., 2011, Meteorit. Planet. Sci., 46, 339
Brown P. G. et al., 2013, Nature, 503, 238
Brown P. G. et al., 2019, Meteorit. Planet. Sci., 54, 2027
Caudron C., Taisne B., Perttu A., Garcés M., Silber E. A., Mialle P., 2016, Geosci. Lett., 3, 26
Ceplecha Z., 1987, Bull. Astron. Inst. Czech., 38, 222
Ceplecha Z., 1996, A&A, 311, 329
Ceplecha Z., McCrosky R. E., 1976, J. Geophys. Res., 81, 6257
Ceplecha Z., Revelle D. O., 2005, Meteorit. Planet. Sci., 40, 35
Ceplecha Z., Borovička J., Elford W. G., Revelle D. O., Hawkes R. L., Porubčan V., Šimek M., 1998, Space Sci. Rev., 84, 327
Colas F. et al., 2014, in Rault J. L., Roggemans P., eds, Proceedings of the International Meteor Conference. The International Meteor Organization, Belgium, IMC 2014, Giron, France, p. 34
Colas F. et al., 2020, A&A, 644, A53
Consolmagno G. J., Britt D. T., 1998, Meteorit. Planet. Sci., 33, 1231
Cooke W. J., Moser D. E., 2012, in Gyssens M., Roggemans P., eds, Proceedings of the International Meteor Conference, 30th IMC. The International Meteor Organization, Belgium, IMC 2012, Sibiu, Romania, p. 9
Devillepoix H. A. R. et al., 2020, Planet. Space Sci., 191, 105036
Drouard A. et al., 2018, A&A, 613, A54
Edwards W. N., Brown P. G., Revelle D. O., 2006, J. Atmos. Sol.-Terr. Phys., 68, 1136
Edwards W. N., Eaton D. W., McCausland P. J., Revelle D. O., Brown P. G., 2007, J. Geophys. Res.: Solid Earth, 112, B10306
Ens T. A., Brown P. G., Edwards W. N., Silber E. A., 2012, J. Atmos. Sol.-Terr. Phys., 80, 208
Gardiol D., Cellino A., Di Martino M., 2016, in Roggemans A. , Roggemans P., eds, Proceedings of the International Meteor Conference. The International Meteor Organization, Belgium, IMC 2016, Egmond, the Netherlands, p. 76
Gi N., Brown P., 2017, Planet. Space Sci., 143, 169
González Á., 2017, J. Seismol., 21, 435
Gritsevich M. I., 2009, Adv. Space Res., 44, 323
Gritsevich M., Koschny D., 2011, Icarus, 212, 877
Gritsevich M. et al., 2014, in Rault J. L., Roggemans P., eds, Proceedings of the International Meteor Conference. The International Meteor Organization, Belgium, IMC 2014, Giron, France, p. 162
Haack H. et al., 2019, Meteorit. Planet. Sci., 54, 1853
Halliday I., Griffin A. A., Blackwell A. T., 1981, Meteoritics, 16, 153
Hankey M., Perlerin V., 2015, in Rault J. L., Roggemans P., eds, Proceedings of the International Meteor Conference. The International Meteor Organization, Belgium, IMC 2015, Mistelbach, Austria, p. 192
Heck P. R. et al., 2020, Meteorit. Planet. Sci., 55, 2341
Hedlin M. A. H., Walker K., Drob D. P., de Groot-Hedlin C. D., 2012, Annu. Rev. Earth Planet. Sci., 40, 327
Hildebrand A. R., McCausland P. J. A., Brown P. G., Longstaffe F. J., Russell S. D. J., Tagliaferri E., Wacker J. F., Mazur M. J., 2006, Meteorit. Planet. Sci., 41, 407
Jeanne S. et al., 2019, A&A, 627, A78
Jenniskens P. et al., 2009, Nature, 458, 485
Jenniskens P., Gural P. S., Dynneson L., Grigsby B. J., Newman K. E., Borden M., Koop M., Holman D., 2011, Icarus, 216, 40
Jenniskens P. et al., 2014, Meteorit. Planet. Sci., 49, 1388
Jenniskens P. et al., 2018, Meteorit. Planet. Sci., 53, 2445
Jenniskens P. et al., 2019, Meteorit. Planet. Sci., 54, 699
Kanamori H., 1977, J. Geophys. Res., 82, 2981
Kikwaya J.-B., Weryk R. J., Campbell-Brown M., Brown P. G., 2010, MNRAS, 404, 387
Koschny D. et al., 2018, in Gyssens M., Rault J. L., eds, Proceedings of the International Meteor Conference. The International Meteor Organization, Belgium, IMC 2017 Petnica, Serbia, p. 10
Koseki M., 2019, eMeteorNews, 4, 220
Kozai Y., 1962, AJ, 67, 591
Le Pichon A., Ceranna L., Pilger C., Mialle P., Brown D., Herry P., Brachet N., 2013, Geophys. Res. Lett., 40, 3732
Marty J., Ponceau D., Dalaudier F., 2010, Geophys. Res. Lett., 37, L19802
Mialle P., Arora N., 2018, in EGU General Assembly Conference Abstracts. European Geosciences Union, EGU General Assembly 2018, Vienna, Austria, p. 11934
Michel P., Thomas F., 1996, A&A, 307, 310
Moilanen J., Gritsevich M., Lyytinen E., 2021, MNRAS, 503, 3337
Moreno-Ibáñez M., Gritsevich M., Trigo-Rodríguez J. M., Silber E. A., 2020, MNRAS, 494, 316
Nedelcu D. A., Birlan M., Popescu M., Bădescu O., Pricopi D., 2014, A&A, 567, L7
Nedelcu D. A. et al., 2018, Rom. Astron. J., 28, 57
Ott U., Herrmann S., Haack H., Grau T., 2010, in 41st Lunar and Planetary Science Conference. Lunar and Planetary Institute, Houston, Texas, p. 1196
Ott T., Drolshagen E., Koschny D., Mialle P., Pilger C., Vaubaillon J., Drolshagen G., Poppe B., 2019, Planet. Space Sci., 179, 104715
Ott T., Drolshagen E., Koschny D., Drolshagen G., Pilger C., Mialle P., Vaubaillon J., Poppe B., 2020, Acta Astronaut., 177, 172
Picone J. M., Hedin A. E., Drob D. P., Aikin A. C., 2002, J. Geophys. Res. (Space Phys.), 107, 1468
Pilger C., Ceranna L., Ross J. O., Le Pichon A., Mialle P., Garcés M. A., 2015, Geophys. Res. Lett., 42, 2523
Pilger C., Gaebler P., Hupe P., Ott T., Drolshagen E., 2020, in EGU General Assembly Conference Abstracts. European Geosciences Union, EGU General Assembly 2020, Online, p. 3290
Popova O., Borovička J., Hartmann W. K., Spurný P., Gnos E., Nemtchinov I., Trigo-Rodríguez J. M., 2011, Meteorit. Planet. Sci., 46, 1525

Rault J.-L., Colas F., 2019, in Pajer U., Rendtel J., eds, Proceedings of the International Meteor Conference. The International Meteor Organization, Belgium, IMC 2019, Bollmannsruh, Germany, p. 112
Rault J.-L. et al., 2018, in Gyssens M., Rault J. L., eds, Proceedings of the International Meteor Conference. The International Meteor Organization, Belgium, IMC 2017, Petnica, Serbia, p. 103
Register P. J., Mathias D. L., Wheeler L. F., 2017, Icarus, 284, 157
Revelle D. O., 1997, Ann. New York Acad. Sci., 822, 284
ReVelle D. O., Whitaker R. W., 1996, Engineering, Construction, and Operations in Space V, vol. 1. American Society of Civil Engineers, Virginia, US, p. 102
Sansom E. K., Bland P., Paxman J., Towner M., 2015, Meteorit. Planet. Sci., 50, 1423
Silber E. A., Brown P. G., 2014, J. Atmos. Sol.-Terr. Phys., 119, 116
Silber E. A., Le Pichon A., Brown P. G., 2011, Geophys. Res. Lett., 38, L12201
Silber E. A., Boslough M., Hocking W. K., Gritsevich M., Whitaker R. W., 2018, Adv. Space Res., 62, 489
Spurný P., Borovička J., Kac J., Kalenda P., Atanackov J., Kladnik G., Heinlein D., Grau T., 2010, Meteorit. Planet. Sci., 45, 1392
Spurný P. et al., 2012, Meteorit. Planet. Sci., 47, 163
Spurný P., Borovička J., Baumgarten G., Haack H., Heinlein D., Sørensen A. N., 2017, Planet. Space Sci., 143, 192
Spurný P., Borovička J., Shrbený L., 2020, Meteorit. Planet. Sci., 55, 376
Subasinghe D., Campbell-Brown M., Stokan E., 2017, Planet. Space Sci., 143, 71
Tancredi G., Motta V., Froeschlé C., 2000, A&A, 356, 339
Toth J. et al., 2018, in Gyssens M., Rault J. L., eds, Proceedings of the International Meteor Conference. The International Meteor Organization, Belgium, IMC 2017, Petnica, Serbia, p. 16
Trigo-Rodriguez J. M., Madiedo J. M., Gural P. S., Castro-Tirado A. J., Llorca J., Fabregat J., Vítek S., Pujols P., 2008, Earth Moon Planets, 102, 231
Vaubaillon J. et al., 2018, in Gyssens M., Rault J. L., eds, Proceedings of the International Meteor Conference. The International Meteor Conference, Belgium, IMC 2017, Petnica, Serbia, p. 53
Vida D., Brown P. G., Campbell-Brown M., Weryk R. J., Stober G., McCormack J. P., 2021, Icarus, 354, 114097
Welten K. C. et al., 2012, Meteorit. Planet. Sci., 47, 186
Yanguas P., Madiedo J. M., Lanchares V., Pagola A., Palacián J. F., Aceituno J., de Guindos E., 2019, in 50th Lunar and Planetary Science Conference. Lunar and Planetary Institute, Houston, Texas, p. 1458

SUPPORTING INFORMATION

Supplementary data are available at *MNRAS* online.

suppl_data

Please note: Oxford University Press is not responsible for the content or functionality of any supporting materials supplied by the authors. Any queries (other than missing material) should be directed to the corresponding author for the article.

APPENDIX A: LOGIC MAP OF THE ALGORITHM USED TO CORRECT THE SATURATION

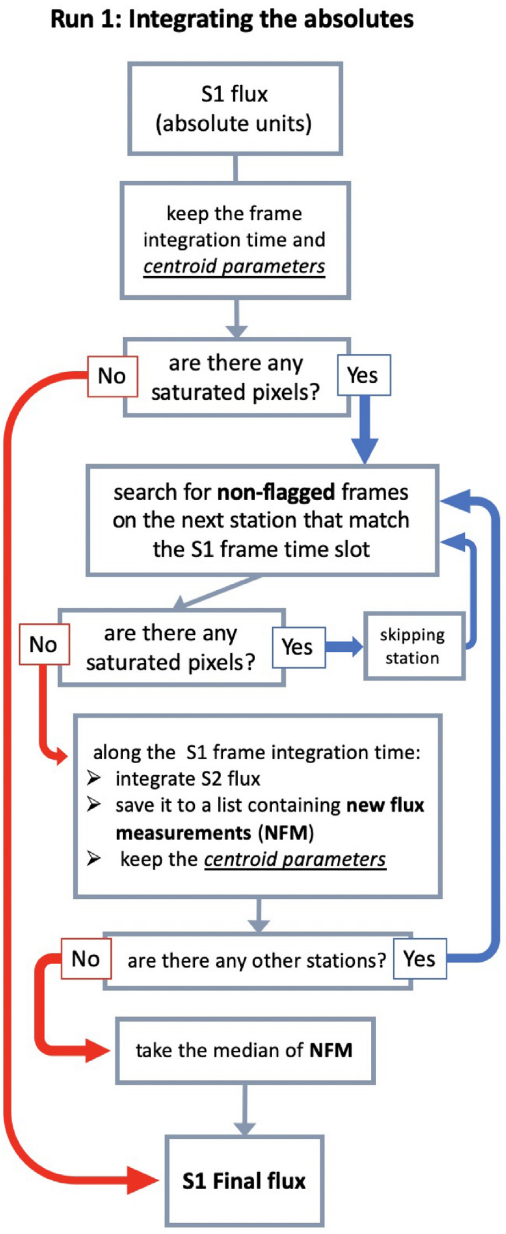

Figure A1. Map used in the first run through the data set, obtained from each frame of every station involved in the detection. All frames are non-flagged by default, as bright events are usually observed by more cameras. The flags on frames (applied by user) become important when analysing events with few cameras, when each obstruction in the CCD-fireball line of sight can take a large toll in the final flux measurement.

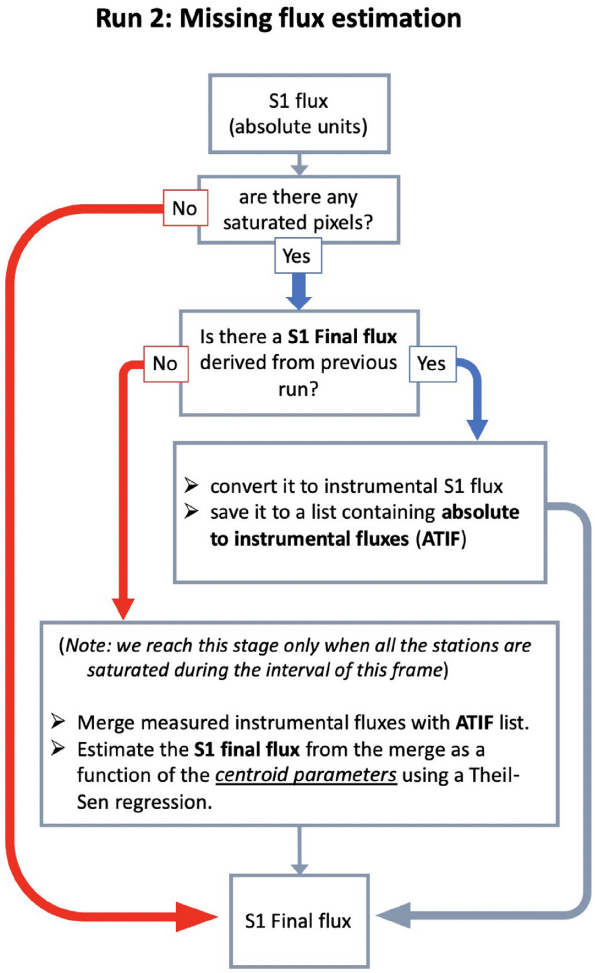

Figure A2. Map of the second run through the data. This will be applied as the first run, to all the frames from all stations. For the few segments where all the stations are saturated it is necessary to obtain a best flux fit on centroid parameters for each station, and assign weights on the final flux for those less saturated. The last step is to run a weighted mean through the final flux from all the stations to obtain the final light curve. The routines are developed in PYTHON open source programming language.

APPENDIX B: SEISMIC SIGNAL

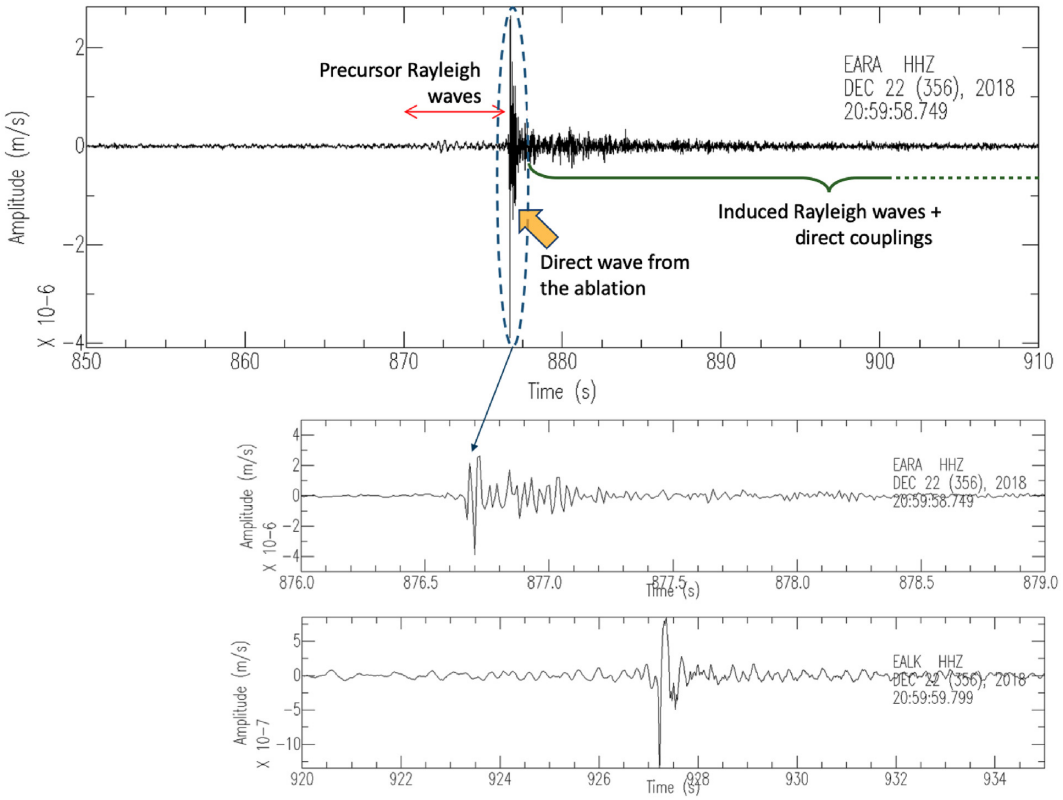

Figure B1. Seismic signals obtained by EARA and EALK stations. EARA, the nearest station, shows first a seismic precursor wave (i.e. the interval along the red arrow). This is generated by the ablation air shock wave coupling with the ground, thus arriving first, as Rayleigh waves. Next, the highest amplitudes (blue dashed circle) correspond to the direct coupling of the shocked air with the surface, at the site of the station. A last wave train (green braces), corresponds to the mixed waves (i.e. direct coupled and surface seismic waves). At the next closest station, EALK, the precursor surface wave and the direct coupling are also observed, but the last wave train mainly show surface seismic wave.

APPENDIX C: ORBIT

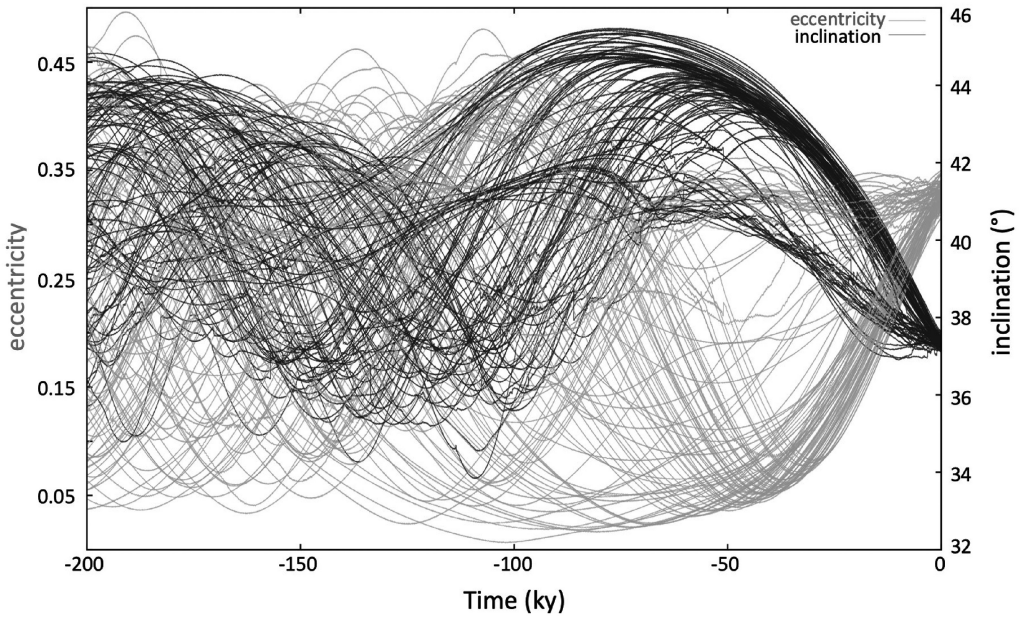

Figure C1. The evolution of eccentricity and inclination of the clones for the last 200 ky. For clarity, only a representative subset of 100 clones is displayed.

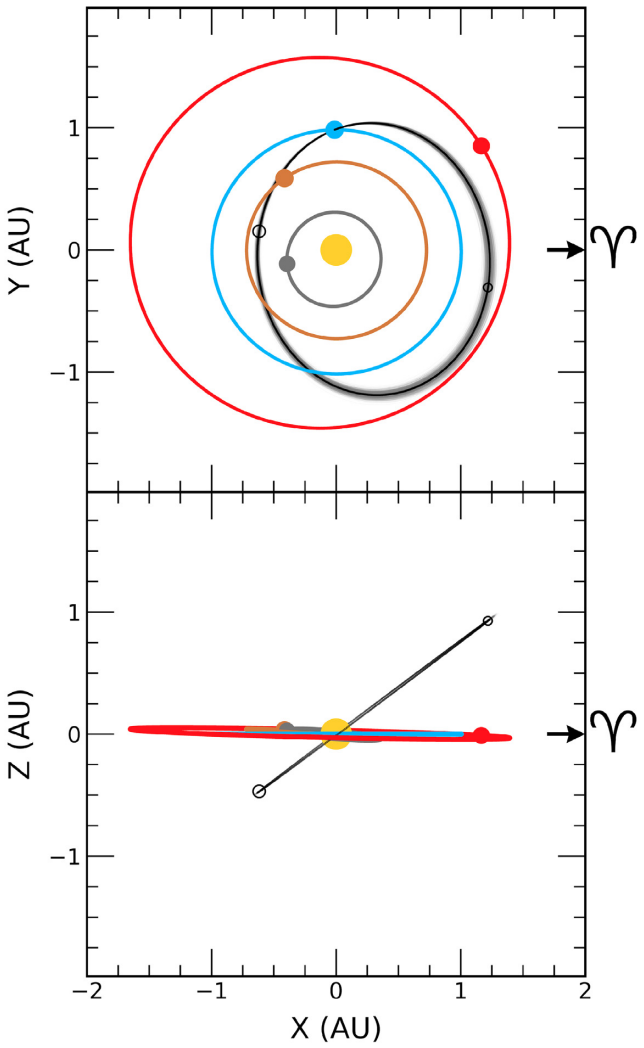

Figure C2. The heliocentric orbit of the meteoroid (black) computed for J2000 as viewed both from top and side. The clones are computed via the Monte Carlo method, sampled within a 3σ uncertainty. The large and small open circles mark the peri- and aphelion position. The terrestrial planets: Mercury (grey), Venus (brown), Earth (blue), Mars (red) and their orbit are also displayed.

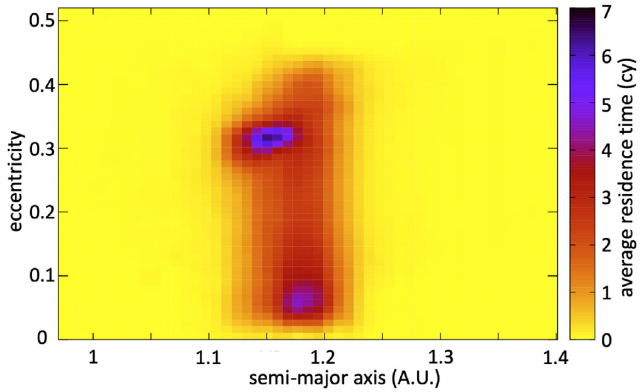

Figure C3. The residence time map (in cy) for the entire (a, e) domain reached during the integration.

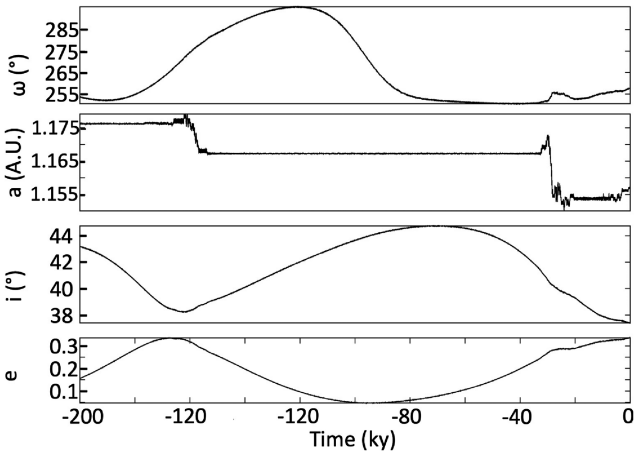

Figure C4. ω, a, i, and e evolution for a clone found in the Kozai–Lidov resonance.

[1]*Astronomical Institute of the Romanian Academy, 5 - Cutitul de Argint Street, 040557 Bucharest, Romania*
[2]*IMCCE, Observatoire de Paris, PSL Research University, CNRS UMR 8028, 77 Av. Denfert-Rochereau, F-75014 Paris Cedex, France*
[3]*Faculty of Physics, University of Bucharest, 405, Atomistilor Street, 077125 Magurele, Ilfov, Romania*
[4]*Division for Medical Radiation Physics and Space Environment, University of Oldenburg, 26129 Oldenburg, Germany*
[5]*European Space Agency, OPS-SP, Keplerlaan 1, NL-2201 AZ Noordwijk, the Netherlands*
[6]*Institut de Minéralogie, Physique des Matériaux et Cosmochimie (IMPMC), Muséum National d'Histoire Naturelle, CNRS UMR 7590, Sorbonne Université, F-75005 Paris, France*
[7]*GEOPS-Géosciences, CNRS, Université Paris-Saclay, F-91405 Orsay, France*
[8]*Service Informatique Pythéas (SIP) CNRS - OSU Institut Pythéas - UMS 3470, Marseille, France*
[9]*Aix Marseille Univ, CNRS, IRD, Coll France, INRA, CEREGE, Aix-enProvence, France*
[10]*Aix Marseille Univ, CNRS, CNES, LAM, Marseille, France*
[11]*Aula EspaZio Gela, Escuela Ingenieria Bilbao, UPV/EHU, E-48013 Bilbao, Spain*
[12]*Departamento Física Aplicada, Universidad País Vasco UPV/EHU, E-48013 Bilbao, Spain*
[13]*Departament de Química, Universitat Autónoma de Barcelona, E-08193 Bellaterra, Catalonia, Spain*
[14]*Institute of Space Sciences (CSIC), Campus UAB, Facultat de Ciències, E-08193 Bellaterra, Barcelona, Catalonia, Spain*
[15]*Institut d'Estudis Espacials de Catalunya (IEEC), E-08034 Barcelona, Catalonia, Spain*
[16]*Institut de Ciències del Cosmos (ICC-UB-IEEC), 1, E-08028 Barcelona, Spain*
[17]*Parc Astronómic Montsec, E-25691 Ager, Spain*
[18]*Laboratori d'Estudis Geofísics Eduard Fontserè, Institut d'Estudis Catalans (LEGEF-IEC), C/Carme 47, E-08001 Barcelona, Catalonia, Spain*
[19]*E.P.S.A. Etablissement public des stations d'altitude 64570 La Pierre Saint Martin, France*
[20]*Académie des sciences, Institut de France, Château Observatoire Abbadia, F-64700 Hendaye, France*
[21]*Observatoire de Dax, Rue Pascal Lafitte, F-40100 Dax, France*
[22]*Université de Bordeaux, CNRS, LOMA, F-33405 Talence, France*

This paper has been typeset from a TEX/LATEX file prepared by the author.